Accepted Manuscript

Dynamic Simulation of Machining Composites Using the Explicit Element-Free Galerkin Method

F. Kahwash, I. Shyha, A. Maheri

Please cite this article as: Kahwash, F., Shyha, I., Maheri, A., Dynamic Simulation of Machining Composites Using the Explicit Element-Free Galerkin Method, *Composite Structures* (2018), doi: https://doi.org/10.1016/j.compstruct. 2018.05.034

Dynamic Simulation of Machining Composites Using the Explicit Element-Free Galerkin Method

[a]F. Kahwash ; [a]I. Shyha[1] and [b]A. Maheri

[a]*Faculty of Engineering and Environment, Northumbria University, Newcastle, UK, NE1 8ST*
[b]*School of Engineering, University of Aberdeen, Aberdeen, UK, AB24 3UE*

Abstract

Machining operations are performed on composite parts to obtain the final geometry. However, machining composites is challenging due to their low machinability and high cost. Numerical modelling of machining presents a valuable tool for cost reduction and a better understanding of the cutting process. Meshfree methods are an attractive choice to model machining problems due to their capability in modelling large deformations. This work presents an explicit meshfree model for orthogonal cutting of unidirectional composites based on the Element-Free Galerkin (EFG) Method. Advantages of the proposed model include: simple and automated preprocessing, advanced material modelling and ability to model high-speed machining. Workpiece material is modelled as orthotropic Kirchhoff material with a choice of three failure criteria: maximum stress, Hashin and LaRC02. Frictional contact calculations are performed based on central differencing, therefore avoiding the use of penalty parameters. Validation of the EFG model is conducted by comparing cutting forces against orthogonal cutting experiments on GFRP samples using a vertical milling machine. It is found that while the numerical cutting forces are in good agreement with experimental ones, the numerical thrust forces are significantly under-estimated. Analysis of failure showed that chip is formed along the fibre direction in the studied range.

[1]Corresponding author email: islam.shyha@northumbria.ac.uk

Keywords: Element-Free Galerkin, Numerical Modelling of Machining, Unidirectional Composites, Cutting Forces, Chip Formation, Progressive Failure

Nomenclature

Δt Time step

Δt_{cr} Critical time step

Γ Boundaries of the computational domain

5   Ω Computational domain

δW^{con} Virtual contact work

δW^{ext} Virtual external work

δW^{int} Virtual internal work

δW^{kin} Virtual kinetic work

10   γ Cutting tool's rake angle

ϕ Shape function vector

μ Contact friction coefficient

ν_{12} Major Poisson's ratio

ν_{21} Minor Poisson's ratio

15   ψ Kink misalginment angle in compressive fibre failure

ρ Density of the body

σ Cauchy stress tensor

σ_i Normal stress component in the ith direction

τ_{12} In-plane shear stress

2

20 θ Fibre orientation angle

$\varUpsilon$ Fracture plane angle

$\varUpsilon_0$ Fracture plane angle in pure transverse compressive loading

ε_1^t Ultimate strain failure in fibre direction (tension)

ε_2^t Ultimate strain failure in transverse direction (tension)

25 φ Shear plane angle

E_1 Young's modulus in fibre direction

E_2 Young's modulus in transverse direction

F_c Main cutting force

F_t Thrust force

30 G_{12} In-plane shear modulus

J Weighted least sqaures functional

N Total number of nodes in the domain

S^l In-plane shear strength

X^c Compression strength in fibre direction

35 X^t Tension strength in fibre direction

Y^c Compression strength in transverse direction

Y^t Tension strength in transverse direction

$\mathbf{A}$ MLS moment matrix

$\mathbf{B}$ The strain matrix

40 $\mathbf{C}$ Material coefficients matrix

$\mathbf{D}$ Damage matrix

3

	$\mathbf{E}$	Green Lagrange strain tensor
	$\mathbf{F}$	Deformation gradient
	$\mathbf{G}$	MLS weighted polynomial matrix
45	$\mathbf{I}$	Identity matrix
	$\mathbf{M}$	Mass matrix
	$\mathbf{S}$	Second Piola Kirchhoff stress tensor
	$\mathbf{T}$	Rotation matrix
	$\bar{\mathbf{t}}$	Prescribed traction on traction boundary
50	$\bar{\mathbf{u}}$	Prescribed displacement on displacement boundary
	$\mathbf{a}$	Acceleration vector
	$\mathbf{b}$	Body forces vector
	$\mathbf{f}^{con}$	Nodal contact force vector
	$\mathbf{f}^{ext}$	Nodal external force vector
55	$\mathbf{f}^{int}$	Nodal internal force vector
	$\mathbf{f}^{kin}$	Nodal kinetic force vector
	$\mathbf{n}$	Outward normal unit coordinate
	$\mathbf{p}$	Polynomial basis function
	$\mathbf{q}$	Unknown MLS coefficients vector
60	$\mathbf{t}$	In-plane tangential unit coordiante
	$\mathbf{u}$	Displacement vector
	$\mathbf{v}$	Velocity vector
	$\mathbf{x}$	Spatial coordinates

4

g Contact gap function

m Number of monomials in a basis functions

n Number of nodes in the DoI

r the cutting ratio

1. Introduction

Increased utilisation of composite products led to increase in machining of composites. Numerical modelling can be used to guide the selection of machining parameters in order to improve machinability of composites [1], while reducing the reliance on expensive experimental approach. Modelling of machining was performed using well-established methods such as the Finite Element Method (FEM). However, recently meshfree methods proved to be a promising candidate in simulating machining process since they are well suited for modelling large deformation and material failure.

Orthogonal cutting is widely used in academic studies of machining (both experimental and numerical) as it provides a good insight into the cutting mechanisms while minimising the geometrical complexities associated with oblique cutting operations. Fibre orientation (θ) is the dominant variable affecting the cutting forces and chip formation mechanisms of unidirectional composites. In the range $0^o < \theta < 90^o$, the chip formation starts with intense local compression leading to compression-induced shear cracking along the fibre-matrix interface reaching to the free surface [2, 3]. The chips usually gets smaller as θ increases [4]. However, they separate parallel to fibre direction [2, 3]. Experimentally, it was found that cutting forces range between local minima at $15^o \leq \theta \leq 30^o$ and a maxima at $\theta = 90^o$. This is explained with increasing of compressive stresses with increased fibre orientations [5].

Meshfree methods are classes of solution techniques of differential equations that do not rely on pre-defined nodal connectivity in constructing the approximated domain. Meshfree methods include: element-free Galerkin (EFG) [6],

5

smoothed particle hydrodynamics (SPH) [7], HP clouds [8], reproducing kernel particle methods [9], radial point interpolation method (RPIM) [10], natural neighbour radial point interpolation method (NNRPIM) [11, 12] and the natu-

95　ral radial element method (NREM) [13, 14] to name a few. Interested readers in the recent advances in meshfree methods should refer to the review of Chen et al. [15]. EFG was proposed in 1994 by Belytschko et al. [6] for elasto-statics and fracture mechanics problems. Subsequently, it was improved and extended to study many other areas such as fluid flow calculations [16], metal forming

100　[17], shells [18, 19], plates and laminates [20, 21]. Recently, a comparison of different meshfree methods (EFG, NNRPIM, NREM) with second order FEM was performed by Belinha et al. [22]. The study compared convergence rate and efficiency of these methods for the analysis of composite plates. It was found that meshfree methods, especially EFG, is of comparable accuracy and

105　efficiency to that of second order FEM. Recently, meshfree methods were applied in modelling composites machining. Iliescu et al. [23] used the discrete element method. The workpiece was modelled as discrete particles with connections. Fibres were modelled as closely joint lines of particles. The model was used to investigate the chipping mechanisms. The method was able to qualitatively

110　capture failure mechanisms at different fibre orientations. SPH method was applied by Shchurov et al. [24] to study UD composites with steel fibres and aluminium matrix. The material was modelled using two distinct Johnson-Cook models. The chip formation was compared with FRP images found in literature. Recently, orthogonal cutting model using the element-free Galerkin method was

115　proposed by Kahwash et al. [25]. The model assumed steady state and compared cutting forces with published experimental and FEM models. The EFG model was of comparable accuracy to the FEM models while the pre-processing phase was simpler. This showed that EFG is promising method in simulating orthogonal cutting.

120　　In developing a machining model, several aspects should be considered carefully, such as simulation type, constitutive model, material failure and contact modelling. A brief description of each follows: Machining simulation can be

6

steady-state or dynamic. Steady-state simulation utilises implicit algorithms while the dynamic uses explicit algorithms. Cutting speed and computational

125 resources should be considered when making this choice. Steady state simulations were utilised in machining simulations at low cutting speeds. Some studies that used steady state approach include [26, 27, 28, 29, 30, 31]. On the other hand, dynamic simulations take the inertial effects into account. This is more suitable for simulating high speed machining. Some studies that used dynamic

130 approach include [32, 33, 34, 35, 36, 37, 38, 39]. The dynamic approach is becoming more popular recently. This is due to the highly dynamic nature of the machining problem, especially at the beginning of the cutting process.

Material modelling is another important aspect of machining simulations. Appropriate choice of constitutive and failure models is essential for accurately

135 predicting cutting force and chip formation. Constitutive models falls under two broad categories: equivalent homogeneous (single phase) and multi-phase material models. The former assumes the material to be one equivalent phase, while the latter models matrix and reinforcement separately with interface elements in between. Most of the single phase models assumed linear elastic constitutive

140 material, such as [26, 27, 29, 31, 25]. However, recently, Zenia [38, 39] assumed a combined elasto-plastic material with isotropic hardening. In multi-phase material model, the fibres are usually modelled as brittle-elastic while the matrix is modelled as elasto-plastic material. Interface elements operate as traction transmitter between the phases. Cohesive zone elements (CZE) are widely used

145 interface elements because they can account for both damage and fracture [1]. Some studies that used multi-phase modelling include [40, 41, 42, 43]. Workpiece material failure is predicted by composite failure theories. Several theories have been used in machining literature such as Tsai-Hill [26, 32, 28], maximum stress [29, 28] and Hashin [29, 33, 35]. On the other hand, some studies [26, 27, 44]

150 combined two failure mechanisms, a primary failure for the onset of chip formation and a secondary for the progression and completion of chip formation. The primary failure model was governed by the shear properties in the cutting zone while the secondary failure was governed by the material failure envelopes.

7

Modelling of machining involves modelling multi-body problem with con-
tact/impact loading. Modelling of contact is challenging since it adds one or
more nonlinearity to the calculations. Usually, it is imposed as a constraint
on the global system equations using some constraint techniques such as the
penalty, Lagrange multiplier or one of their different variations. Several works
studied contact phenomena using the Element-free Galerkin. A frictionless
penalty formulation for elasto-statics was proposed in [45]. A contact detection
algorithm designed for meshfree methods was proposed in [46] based on the
moment matrix. The proposed algorithm was successfully applied to RKPM
simulation of Taylor Impact bar. Li et al. [17] developed a procedure for con-
tact impact problems utilising the EFG method and stress-point integration in
discretising the weak form. Furthermore, an algorithm for contact calculations
based on the central difference method at the contact interface. The proposed
formulation is applied in metal forming applications with benchmark tests such
as Taylor impact bar and backward extrusion. Xiong et al. [47] applied the EFG
to the problem of plain strain rolling. They developed a rigid-plastic material
model for slightly compressible materials and found that the EFG was capable
of describing the velocity field discontinuity near the roller edges.

In this paper, a model to simulate the orthogonal cutting of unidirectional
composites using the Explicit EFG method is proposed. The main outputs of
interest are the cutting forces and chip formation at positive fibre orientations.
Theoretical model development is presented first followed by numerical imple-
mentation of the model and experimental procedure for validating force results.
Then cutting forces and chip formation predictions using different failure criteria
are presented and discussed.

2. The Explicit Element Free Galerkin Model

This section describes the development of the mathematical model of orthog-
onal cutting of composites. We start by developing the continuum mechanics
model then deriving the discretised system equations in space and time. Aux-

iliary models such as contact force calculations and material modelling are also presented.

₁₈₅ *2.1. Governing Equations*

Consider a solid body at time $t = 0$ occupying a reference configuration Ω_0 and bounded by Γ_0. The body is then subjected to forces, which create a displacement field **u**. At time t, the current configuration is Ω_t and the boundaries are Γ_t. In order to determine the state of the body at time t, we ₁₉₀ start with the conservation of momentum equation in its differential form

$$\bigtriangledown \cdot \sigma - \mathbf{b} = \rho \mathbf{a} \tag{1}$$

where, σ is the stress field, **b** is the body force tensor, ρ is the density of the material and **a** is the acceleration of the body. Equation (1) is subject to the following traction and displacement boundary conditions:

$$n_j \sigma = \bar{\mathbf{t}} \quad \text{on} \quad \Gamma_t \tag{2}$$

$$u_i = \bar{u}_i \quad \text{on} \quad \Gamma_u \tag{3}$$

where Γ_t and Γ_u are traction and displacement boundaries respectively. In ₁₉₅ addition, Equation (1) is subject to the following initial conditions

$$\mathbf{u}(\mathbf{x}_0, 0) = \mathbf{u}_0(\mathbf{x}_0) \tag{4}$$

$$\sigma(\mathbf{x}_0, 0) = \sigma_0(\mathbf{x}_0) \tag{5}$$

The weak form of Equation (1) is obtained by multiplying the differential form by a kinematically admissible, virtual displacement field $\delta \mathbf{u}$ and integrating over the current configuration Ω_t [48]. After integration by parts and rearranging we obtain:

$$\int_{\Omega_t} \delta \varepsilon^T \sigma \, \mathrm{d}\Omega - \int_{\Omega_t} \delta \mathbf{u}^T \mathbf{b} \, \mathrm{d}\Omega - \int_{\Gamma_t} \delta \mathbf{u}^T \bar{\mathbf{t}} \, \mathrm{d}\Gamma - \int_{\Omega_t} \rho \, \delta \mathbf{u}^T \, \mathbf{a} \, \mathrm{d}\Omega = 0 \tag{6}$$

₂₀₀ where, $\delta \varepsilon^T = \frac{\partial(\delta \mathbf{u}^T)}{\partial \mathbf{x}}$ is the spatial variation of the strain field. Equation (6) cannot be evaluated as it refers to the current (unknown) configuration of the

9

body Ω_t. Integration domain can be changed from Ω_t to a known configuration using an appropriate stress and strain measures [49]. To achieve this, two main approaches are used, namely, total Lagrangian formulation or updated
205 Lagrangian formulation. In the former, the integration domain is changed to Ω_0, while in the latter, the integration domain is changed to the last known configuration Ω_{t-1}.

In this study, the Updated Lagrangian formulation is adopted. This is due to the presence of contact forces, which should be calculated with reference to the deformed configuration rather than the un-deformed [48]. Furthermore, Second Piola Kirchhoff stress and Green-Lagrange strain are used. These measures are suitable for describing geometrical non-linearity and are widely used in nonlinear solid mechanics problems that involve large deformations. Second Piola Kirchhoff stress $\mathbf{S}$ is related to Cauchy (nominal) stress by

$$\mathbf{S} = \det(\mathbf{F})\mathbf{F}^{-1} \cdot \sigma \cdot \mathbf{F}^{-\mathrm{T}} \tag{7}$$

where, $\mathbf{F}$ is the deformation gradient. The Green-Lagrange strain tensor is defined as follows

$$\mathbf{E} = \frac{1}{2}(\mathbf{F}^T \cdot \mathbf{F} - \mathbf{I}) \tag{8}$$

where, $\mathbf{I}$ is the identity matrix.

Now we can rewrite Equation (6) as follows:

$$\underbrace{\int_{\Omega_\mathrm{r}} \delta\mathbf{E}^T\,\mathbf{S}\,\mathrm{d}\Omega}_{\delta\mathrm{W}^{\mathrm{int}}} - \underbrace{\int_{\Omega_\mathrm{r}} \delta\mathbf{u}^T\mathbf{b}\,\mathrm{d}\Omega - \int_{\Gamma_\mathrm{r}} \delta\mathbf{u}^T\bar{\mathbf{t}}\,\mathrm{d}\Gamma}_{\delta\mathrm{W}^{\mathrm{ext}}} + \underbrace{\int_{\Omega_\mathrm{r}} \rho\,\delta\mathbf{u}^T\mathbf{a}\,\mathrm{d}\Omega}_{\delta\mathrm{W}^{\mathrm{kin}}} = 0 \tag{9}$$

where, $\Omega_r \equiv \Omega_0$ for total Lagrangian formulation and $\Omega_r \equiv \Omega_{t-1}$ for updated
210 Lagrangian formulation. Equation (9) can be viewed as a the principle of virtual work and each of the terms can be given a physical interpretation as follows: δW^{int} is the virtual internal work, δW^{ext} is the virtual external work and δW^{kin} is the virtual kinetic work.

2.2. Meshfree Approximation

The meshfree spatial discretisation is achieved through Moving Least Squares (MLS) approximation [6, 50, 51]. Consider a continuous field variable $u(\mathbf{x})$ de-

10

fined in the domain Ω. A discrete approximation u^h can be formulated as follows:

$$u^h(\mathbf{x}) = \sum_j^m p_j(\mathbf{x})q_j(\mathbf{x}) \equiv \mathbf{p}^T(\mathbf{x})\mathbf{q}(\mathbf{x}) \tag{10}$$

where, $\mathbf{p}$ is a complete polynomial basis function with m monomial terms, $\mathbf{q}(\mathbf{x})$ is a vector of unknown coefficients. A complete polynomial linear basis function in 2D is given as:

$$\mathbf{p}^T(\mathbf{x}) = \left\{ 1 \quad x \quad y \right\}, \quad m = 3 \tag{11}$$

The unknown coefficients $q_j(x)$ in Equation 10 can be calculated by minimising the difference between the local approximation and the function through a weighted least-squares fit, which gives:

$$J = \sum_I^n w(\mathbf{x} - \mathbf{x}_I)[\mathbf{p}^T(\mathbf{x})\mathbf{q}(\mathbf{x}) - \mathbf{u}_I]^2 \tag{12}$$

215 where n is the number of points in the neighbourhood of $\mathbf{x}_I$ for which the weight function $\mathbf{w}(\mathbf{x} - \mathbf{x}_I) \neq 0$, and $\mathbf{u}_I$ is the nodal value of $\mathbf{u}$ at $\mathbf{x} = \mathbf{x}_I$.

Equation 12 can be re-written as follows

$$J = (\mathbf{P}\,\mathbf{q} - \mathbf{u})^T \mathbf{W}(\mathbf{x})(\mathbf{P}\,\mathbf{q} - \mathbf{u}) \tag{13}$$

where,

$$\mathbf{u}^T = \left\{ u_1 \quad u_2 \quad \cdots \quad u_n \right\}$$

$$\mathbf{P} = \begin{bmatrix} p_1(x_1) & p_2(x_1) & \cdots & p_n(x_1) \\ p_1(x_2) & p_2(x_2) & \cdots & p_n(x_2) \\ \vdots & \vdots & \ddots & \vdots \\ p_1(x_n) & p_2(x_n) & \cdots & p_n(x_n) \end{bmatrix}$$

$$\mathbf{W}(\mathbf{x}) = \begin{bmatrix} w(x - x_1) & 0 & \cdots & 0 \\ 0 & w(x - x_2) & \cdots & 0 \\ \vdots & \vdots & \ddots & \vdots \\ 0 & 0 & 0 & w(x - x_n) \end{bmatrix}$$

11

$q_j(\mathbf{x})$ is obtained by differentiating Equation 13 with respect to $\mathbf{q}$ and finding the stationary point

$$\frac{\partial J}{\partial \mathbf{q}} = (\mathbf{P}\ \mathbf{q} - \mathbf{u})^T \mathbf{W}(\mathbf{x}) = \mathbf{0} \tag{14}$$

Therefore, $\mathbf{q}$ is given as

$$\mathbf{q} = \mathbf{A}^{-1}\ \mathbf{G}\ \mathbf{u} \tag{15}$$

where, $\mathbf{A} = \mathbf{P}^T\ \mathbf{W}(\mathbf{x})\ \mathbf{P}$ is called the moment matrix and $\mathbf{G} = \mathbf{P}^T\ \mathbf{W}(\mathbf{x})$. From the above, the final MLS approximation relationship is obtained

$$u^h(\mathbf{x}) = \sum_{I=1}^{n} \phi_I(\mathbf{x}) u_I \quad = \phi(\mathbf{x})\mathbf{u} \tag{16}$$

The shape function $\phi(\mathbf{x})$ is defined by

$$\phi(\mathbf{x}) = \sum_{j=0}^{m} p_j(\mathbf{x})(\mathbf{A}^{-1}(\mathbf{x})\mathbf{G}(\mathbf{x}))_j = \mathbf{p}^T \mathbf{A}^{-1}\mathbf{G} \tag{17}$$

The partial derivatives of $\phi_I(\mathbf{x})$ can be obtained as follows

$$\phi_{,i} = \sum_{j}^{m}\{p_{j,i}(\mathbf{A}^{-1}\mathbf{G})_j + p_j(\mathbf{A}_{,\mathbf{i}}^{-1}\mathbf{G}) + (\mathbf{A}^{-1}\mathbf{G}_{,\mathbf{j}})_j\} \tag{18}$$

where the index that follows a comma is a spatial derivative and

$$\mathbf{A}_{,\mathbf{i}}^{-1} = -\mathbf{A}^{-1}\mathbf{A}_{,\mathbf{i}}\mathbf{A}^{-1} \tag{19}$$

An important aspect of the meshfree shape function calculations is the choice of the weight function. Different weight functions were proposed in literature e.g. exponential, high-order splines and others. The weight function used in this study is a regularised weight function proposed by Most [52]. It approximately possesses the Kronecker-delta property, which is inherited by the shape function. This makes imposing of displacement boundary conditions possible without the need for using constraints methods such as penalty or Lagrange multiplier. The regularised weight function is given as:

$$w_R(d_i) = \frac{\tilde{w}_R(d_i)}{\sum_{j=1}^{m} \tilde{w}_R(d_j)} \tag{20}$$

$$\tilde{w}_R(d) = \frac{\left(\left(\frac{d}{D}\right)^2 + \omega\right)^{-2} - (1+\omega)^{-2}}{\omega^{-2} - (1+\omega)^{-2}}; \quad \omega \ll 1 \tag{21}$$

where, d is the distance between the point of interest and the support node, m is the number of nodes within the domain of influence, D is the size of the domain of influence and ω is a constant that is usually much smaller than one.

220 In this study $\omega = 10^{-5}$ is used following the recommendations of Most et al. [52].

2.3. Discretisation of Governing Equations

Using the meshfree MLS approximation, the continuum equation (9) can be changed into spatially discretised equations. Firstly, the displacement-strain

225 relationship has to be discretised followed by discretisation of the weak form terms. Finally, temporal discretisation of the semi-discrete equations become possible.

2.3.1. Displacement-Strain Equations

In this study, we consider a plane stress problem of orthotropic materials. Hence, Green Lagrange strain tensor can be represented in Voigt notation as a vector:

$$\mathbf{E}^T = \left\{ E_{xx} \qquad E_{yy} \qquad E_{xy} \right\} \tag{22}$$

The 2D displacement field $\mathbf{u}^T = \left\{ u_x \qquad u_y \right\}$ can be approximated at a point of interest using MLS shape functions as follows

$$\mathbf{u} = \sum_I^n \phi_I \mathbf{u}_I \tag{23}$$

where ϕ is the MLS shape function, n the number of nodes in the support domain of the point of interest. This leads to

$$\delta \mathbf{u} = \sum_I^n \phi_I \delta \mathbf{u}_I \tag{24}$$

The strain can be discretised as follows

$$\mathbf{E} = \sum_I^n \nabla \phi_I \mathbf{u}_I = \sum_I^n \mathbf{B}_I \mathbf{u}_I \tag{25}$$

13

where $\mathbf{B}$ is called the strain matrix. The virtual strain caused by the virtual displacement field is approximated as follows

$$\delta \mathbf{E} = \sum_I^n \mathbf{B}_I \delta \mathbf{u}_I \tag{26}$$

The strain-displacement matrix is given below

$$\mathbf{B} = \begin{bmatrix} F_{11}\frac{\partial \phi_1}{\partial x} & F_{21}\frac{\partial \phi_1}{\partial x} & \cdots \\ F_{12}\frac{\partial \phi_1}{\partial y} & F_{22}\frac{\partial \phi_1}{\partial y} & \cdots \\ F_{11}\frac{\partial \phi_1}{\partial y} + F_{12}\frac{\partial \phi_1}{\partial x} & F_{21}\frac{\partial \phi_1}{\partial y} + F_{22}\frac{\partial \phi_1}{\partial x} & \cdots \end{bmatrix} \tag{27}$$

In case of small displacement, $\mathbf{F} \approx \mathbf{I}$ and $\mathbf{B}$ becomes equivalent to the well-

230   known strain matrix for small displacement linear elasticity.

2.3.2. Discretisation of the Virtual Work Terms

Using the MLS shape function and its derivatives in addition to the strain-displacement relations, each term in Equation (9) can be discretised spatially as follows:

$$\delta W^{int} = \int_{\Omega_r} \delta \mathbf{E}^T \mathbf{S}_I \ \mathrm{d}\Omega = \int_{\Omega_r} \sum_I^n \mathbf{B}_I^T \delta \mathbf{u}_I^T \mathbf{S}_I \ \mathrm{d}\Omega \tag{28}$$

In order to complete the equation development for the entire domain, the summation above should be re-written with respect to the global nodal numbering $(1 \rightarrow N)$. Due to the local support property of the MLS shape function. This change can be readily made. This means that the contributions of the points outside the domain of influence will be zero. Therefore Equation (28) becomes

$$\delta W^{int} = \int_{\Omega_r} \sum_I^N \mathbf{B}_I^T \delta \mathbf{u}_I^T \mathbf{S}_I \ \mathrm{d}\Omega = \sum_I^N \delta \mathbf{u}_I^T \int_{\Omega_r} \mathbf{B}_I^T \mathbf{S}_I \ \mathrm{d}\Omega \tag{29}$$

We denote the local nodal internal force as follows

$$\mathbf{f}_I^{int} = \int_{\Omega_r} \mathbf{B}_I^T \mathbf{S}_I \ \mathrm{d}\Omega \tag{30}$$

Equation (28) becomes

$$\delta W^{int} = \sum_I^N \delta \mathbf{u}_I^T \mathbf{f}_I^{int} \tag{31}$$

14

Now we can generalise the above formulation for the entire domain by applying the summation over all the nodes in the domain and collecting the contributions in global matrices as follows

$$\delta\hat{\mathbf{u}} = \sum_I^N \delta\mathbf{u}_I \qquad \mathbf{f}^{int} = \sum_I^N \mathbf{f}_I^{int} \tag{32}$$

Therefore

$$\delta W^{int} = \delta\hat{\mathbf{u}}^T \mathbf{f}^{int} \tag{33}$$

Using similar procedure we can discretise the external virtual work:

$$\delta W^{ext} = \int_\Omega \delta\mathbf{u}^T \mathbf{b}\mathrm{d}\Omega + \int_{\Gamma_t} \delta\mathbf{u}^T \bar{\mathbf{t}}\mathrm{d}\Gamma = \int_\Omega \sum_I^N \phi_I^T \delta\mathbf{u}_I^T \mathbf{b}\mathrm{d}\Omega + \int_{\Gamma_t} \sum_I^N \phi_I^T \delta\mathbf{u}_I^T \bar{\mathbf{t}} \ \mathrm{d}\Gamma$$

$$= \sum_I^N \delta\mathbf{u}_I^T \underbrace{\left[\int_\Omega \phi_I^T \mathbf{b}\mathrm{d}\Omega + \int_{\Gamma_t} \phi_I^T \bar{\mathbf{t}} \ \mathrm{d}\Gamma \right]}_{\mathbf{f}_I^{ext}} = \delta\hat{\mathbf{u}}^T \mathbf{f}^{ext}$$

$$\tag{34}$$

The kinetic term is discretisted following the same argument as the previous two components

$$\delta W^{kin} = \int_\Omega \delta\mathbf{u}^T \rho\ddot{\mathbf{u}}\mathrm{d}\Omega = \int_\Omega \sum_I^N \phi_I^T \delta\mathbf{u}_I^T \rho \sum_J^N \phi_J \mathbf{a}_J \mathrm{d}\Omega$$

$$= \sum_I^N \sum_J^N \delta\mathbf{u}_I^T \underbrace{\int_\Omega \phi_I^T \rho \ \phi_J \mathrm{d}\Omega}_{M_{IJ}} \mathbf{a}_J = \delta\hat{\mathbf{u}}^T \mathbf{M}\mathbf{a} \tag{35}$$

By combining Equations [31, 34, 35] we obtain

$$\delta\hat{\mathbf{u}}^T \left(\mathbf{f}^{int} - \mathbf{f}^{ext} + \mathbf{M}\mathbf{a} \right) = 0 \tag{36}$$

235 Equation (36) can now be discretised in time. In this study, the central difference method is utilised. Using lumped mass matrix and suitable timestep (refer to Section (3.2)), the solution can be obtained without system equations inversion, which makes the implementation computationally more efficient.

15

2.4. Contact-Impact

Machining simulations are multi-body problems with contact between the cutting tool and the workpiece. As such, contact force calculations need to be added to the model. Modelling contact is a challenging task since the contact boundaries are part of the solution (i.e. not known a priori). This adds *boundary non-linearity* to the problem in addition to the geometrical and material non-linearity [53]. Kinematic contact condition is imposed on the system, which states that two material points cannot occupy the same space at the same time. This can be formalised by the use of gap function as follows:

$$g(\mathbf{x}) \leq 0 \tag{37}$$

The gap function of discretised system is defined in matrix form as

$$g_i = (\mathbf{x}^S - \mathbf{x}^M) \cdot \mathbf{i} \; ; \quad i = [n, \, t] \; ; \quad \mathbf{i} = [\mathbf{n}, \, \mathbf{t}] \tag{38}$$

240 A convenient way of studying contact problems is the "master-slave" approach, where the master body is considered rigid body and applying the kinematic contact condition on any slave nodes that penetrate a master segment. A basic terminology of contact is illustrated in Figure (1)
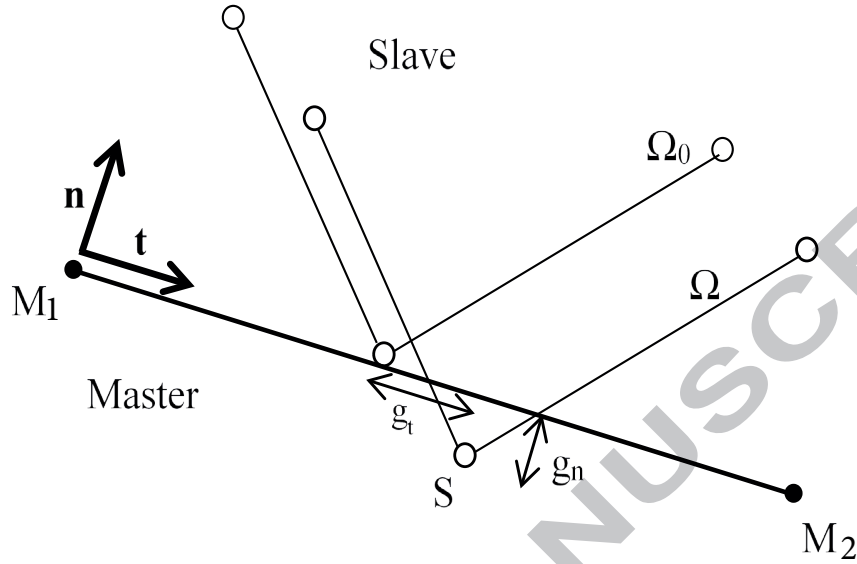
16

Figure 1: Basic Contact Terminology [[25]]

The nodal contact forces are calculated using central difference scheme as follows [46, 54]: The normal force acting on the slave nodes due to penetration of a master segment (frictionless contact) is given as:

$$f_{n,j}^{con} = \frac{2M_{s(j)}g_j}{(\Delta t)^2} \cdot \mathbf{n} \tag{39}$$

where, Δt is the time step and $M_{s(j)}$ is the mass of the penetrating slave node, which is calculated using the mass expression in Equation 35 during the assembly of the system equations in the preprocessing stage. By utilising Coloumb friction law, we can calculate the tangential contact force in terms of relative velocity of contacting slave/master v_r or in terms of the tangential gap. For stick conditions

$$f_{t,j}^{con} = \frac{M_{s(j)}v_{r(j)}}{\Delta t} \cdot \mathbf{t} = \frac{M_{s(j)}g_{t,j}}{(\Delta t)^2} \tag{40}$$

For slip condition:

$$f_{t,j}^{con} = \mu f_{n,j}^{con} \tag{41}$$

In order to decide which contact condition applies, two trial tangential forces are calculated using Equations 40 and 41. If the trial stick force is smaller than

17

trial slip force, then the contact segment is considered to be in stick condition; otherwise slip condition is applied. The contact force is then updated accordingly. Thus, the contact force acting on each slave node j can be calculated for stick condition

$$f_j^{con} = \frac{M_{s(j)}}{(\Delta t)^2} \left(2g_j \cdot \mathbf{n} + g_j \cdot \mathbf{t}\right) \tag{42}$$

and for slip condition

$$f_j^{con} = \frac{2M_{s(j)}}{(\Delta t)^2} \; g_j \cdot \mathbf{n} \; (1 + \mu) \tag{43}$$

The contact nodal forces calculated in Eqns (42, 43) should be added to the virtual work in order to obtain the final spatially discretised form of the virtual work equation.

$$\delta W^{con} = \int_{\Gamma_c} \mathbf{f} \; \delta \mathbf{u}^T \mathrm{d}\Gamma = \int_{\Gamma_c} \sum_j^m f_j \delta \mathbf{u}^T \mathrm{d}\Gamma = \sum_j^m f_j \sum_I^P (\phi_I \delta \mathbf{u}_I^T) \tag{44a}$$

$$= \sum_I^P \left(\phi_I \sum_j^m f_j \right) \delta \mathbf{u}_I^T = \sum_I^P \bar{f}_j \; \delta \mathbf{u}_I^T = \mathbf{f}^{con} \; \delta \hat{\mathbf{u}}^T \tag{44b}$$

The last term can be added to Equation [36] to obtain

$$\delta \hat{\mathbf{u}}^T \left(\mathbf{f}^{int} - \mathbf{f}^{ext} - \mathbf{f}^{con} + \mathbf{M}\mathbf{a} \right) = 0 \tag{45}$$

Since $\delta \mathbf{u}^T$ is arbitrary, it follows that:

$$\mathbf{M}\mathbf{a} = \mathbf{f}^{ext} + \mathbf{f}^{con} - \mathbf{f}^{int} \tag{46}$$

Practically, distributing the local contact forces into the global contact force vector using the shape function is not required in this case. This is a consequence of the almost-interpolating property of the shape function combined with the force calculations at the nodes (not at quadrature points). However, it is kept to maintain the generality of the algorithm and in the case of using weight functions that do not have interpolating properties. It is worth noting that the above nodal force calculations given in Equations (42, 43), are equivalent to penalty method with variable penalty parameter. The "penalty parameter" is calculated from the mass of the node and timestep of the algorithm. This has

18

an advantage from numerical implementation point-of-view, as the same contact algorithm can be used with implicit and explicit solvers and only the "penalty parameter" value would change. In implicit algorithms, mass and time steps are usually not calculated, a constant penalty parameter can be used. Choosing penalty parameter is usually requires numerical experiments [55]. However, in the case of explicit algorithm such as the proposed model, choosing the penalty parameter is avoided without adding extra unknowns to the system (e.g. as in Lagrange multiplier).

2.5. Temporal Integration

Equation [46] is called the semi-discrete equation because it is discrete in space but not in time. The central difference method is used to discretise in time. It is commonly used method in nonlinear solid mechanics. The temporal quantities, i.e. velocity and acceleration are calculated based on the central differencing formulae. The equations and procedure presented by Belytschko et al. [56] are adopted in this work. Time increments are divided into half steps, which enable energy balance calculations. The simulation time t^n varies between 0 and T. The time increment quantities are

$$\Delta t^{n+^1/_2} = t^{n+1} - t^n \; ; \quad t^{n+^1/_2} = 0.5(t^{n+1} + t^n) \; ; \quad \Delta t^n = t^{n+^1/_2} - t^{n-^1/_2} \quad (47)$$

The velocity at the first half time step $\mathbf{v}^{n+^1/_2}$ can be calculated using the acceleration of the previous time step as follows:

$$\mathbf{v}^{n+^1/_2} = \mathbf{v}^n + (t^{n+^1/_2} - t^n)\mathbf{a}^n \quad (48)$$

After that, displacement at increment $n+1$ can be calculated from $\mathbf{v}^{n+^1/_2}$ as follows

$$\mathbf{u}^{n+1} = \mathbf{u}^n + \Delta t^{n+^1/_2}\mathbf{v}^{n+^1/_2} \quad (49)$$

One of the main features of the CDM is that acceleration $\mathbf{a}^{n+1}$ can be calculated using all known quantities at time t^n as per Equation 46. Once the new acceleration is calculated, the second velocity update can be obtained using the

19

following formula:

$$\mathbf{v}^{n+1} = \mathbf{v}^{n+1/2} + (t^{n+1} - t^{n+1/2})\mathbf{a}^{n+1} \tag{50}$$

The details of the numerical implementation of these equations are presented in Section 3.6.

2.6. Material Modelling

265   In this section, a novel material model is developed. It consists of two main parts: the constitutive equations that describe the pre-failure material behaviour and progressive failure model that predicts the onset and propagation of failure in the workpiece material.

2.6.1. Constitutive Equations

The material behaviour before failure is modelled using *Saint Venant-Kirchhoff* material model [48], which is an extension of linear elastic behaviour while taking into account the nonlinear components of stress and strain (using Green Lagrange strain and PK2 stress). The material model is written as follows:

$$\mathbf{S} = \mathbf{C}\,\mathbf{E} \tag{51}$$

270   This material model can describe fully anisotropic material [48], so it is capable of dealing with orthotropic materials.

2.6.2. Progressive Material Failure

In this work, three failure criteria are used, namely, maximum stress, Hashin and LaRC02 failure. Summary of their equations is given in Appendix A. Stress in local coordinates is required for failure calculations. The local stress can be retrieved from global stress using the following relation:

$$\mathbf{S}_{12} = \mathbf{T} \cdot \mathbf{S}_{xy} \tag{52}$$

where, $\mathbf{S}_{12}$ is the local stress, $\mathbf{S}_{xy}$ and $\mathbf{T}$ is the rotation matrix given by:

$$\mathbf{T} = \begin{bmatrix} c^2 & s^2 & 2sc \\ s^2 & c^2 & -2sc \\ -sc & sc & c^2 - s^2 \end{bmatrix} \tag{53}$$

20

where, $c = cos(\theta)$ and $s = sin(\theta)$.

Failure envelopes for the workpiece material used in experiments using the
275 different failure criteria is given in Figure 3. Maximum stress and Hashin criteria
have been used before in the modelling of machining composites e.g. [33, 29, 25].
LaRC02 was developed by Dàvila et al. [57] of NASA and named after Langley
Research Centre. It is based on Puck's action plane concept [58] combined with
concepts proposed by Hashin [59]. The aim was to develop failure criteria that
280 does not rely on experimental parameters but based on physical understand-
ing of the composite lamina failure. LaRC02 was chosen in this work for the
following reasons:

- It can account for the positive effect of transverse compression on the shear
  strength of unidirectional lamina.

285 - It corresponds well with the experimental evidence of the World Wide
  Failure Exercise.

- It does not contain empirical parameters/tuning parameters.

- While newer versions of LaRC02 were later developed (LaRC03 and LaRC04),
  they require additional material testing and are more complicated to im-
290 plement.

Progression of failure is modelled using stiffness degradation concept whereby
the stiffness of the material point is degraded selectively based on the type of
failure. The stiffness degradation procedure and parameters are similar to the
one used in [25]. A normalised damage matrix $\mathbf{D}$ is used to store the damage
295 status of the integration points at each time step. For each integration point, 3
damage values are stored, namely, fibre, matrix and interface. These values are
calculated from one of the failure criteria mentioned above. The value of the
damage parameter varies between 0 (no damage) to 1 (complete damage).

3. Numerical Implementation

300 The proposed model is implemented in MATLAB® code; (refer to subsection
3.6). This section describes some aspects of the code implementation including

21

model settings, critical time step calculations and material parameters.

3.1. Numerical Integration of the Weak Form Terms

Numerical integration of the weak form terms is performed using Gaussian quadrature over background mesh. The integral is converted into a sum over the integration points of the cell. For example, integration of the internal nodal force can be performed as follows: Assuming that the domain is covered by n_c cells, in each cell there are n_G integration points at positions $\mathbf{x}_G$; Equation (30) becomes:

$$\mathbf{f}_I^{int} = \int_{\Omega_r} \mathbf{B}_I^T \mathbf{S}_I \ \mathrm{d}\Omega = \sum_{k}^{n_c} \sum_{i}^{n_G} \varpi_i \mathbf{B}_I(\mathbf{x}_{Gi}) \mathbf{S}_I(\mathbf{x}_{Gi}) |\mathbf{J}_{ik}| \tag{54}$$

where, ϖ_i is the weighting factor for Gauss point at $\mathbf{x}_{Gi}$ and $|\mathbf{J}_{ik}|$ is the determinant of the Jacobian matrix of the kth background cell. Throughout this study, 2×2 Gauss points per cell are used. This was found to give best performance as higher number of integration points tended to increase numerical noise in the solution.
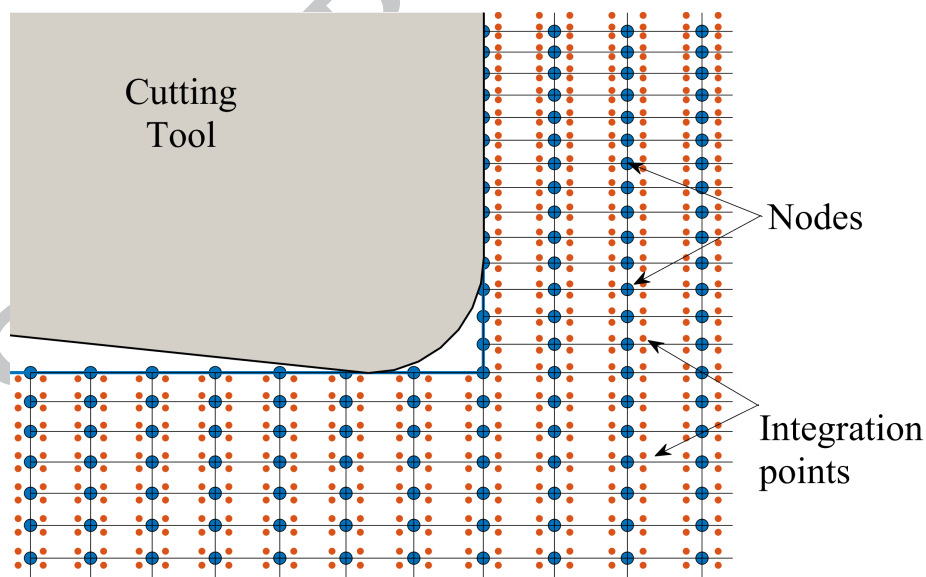

Figure 2: Close up near the cutting edge showing the nodal distribution (blue points) and Gauss integration points (red points) within the background mesh (black)

22

3.2. Critical Time Step

The central difference method is only conditionally stable [48, 49, 60]. This means that a robust algorithm should have an automatic time step calculation. The critical time step is related to the stress wave propagation speed. This is a function of the material density and mechanical properties as well as the distance between discretisation nodes. Unlike isotropic material, a composite laminate has several *phase velocities*. The maximum velocity is used in critical time step calculations [61]

$$c_{max} = \sqrt{C_{11}/\rho} \; ; \quad \text{where } C_{11} = \frac{E_1}{1 - \nu_{12} \; \nu_{21}} \tag{55}$$

$$\Delta t_{cr} < \frac{\min(dist)}{c_{max}} \tag{56}$$

310 where, *dist* is the distance between nodes.

3.3. Material Failure Parameters

In order to estimate the shear and normal strength in the cutting zone, we use the merchant model. Using principle force components, shear and normal stress components acting on the shear plane can be calculated as per the following well-known relations

$$F_s = F_c \; cos(\varphi) - F_t \; sin(\varphi) \tag{57}$$

$$F_{ns} = F_c \; sin(\varphi) + F_t \; cos(\varphi) \tag{58}$$

where, F_c and F_t are the cutting and thrust forces respectively, which can be obtained from experiments using force dynamometer, and φ is the shear plane angle, which is given as follows:

$$\varphi = \tan^{-1} \frac{r \cos \gamma}{1 - r \sin \gamma} \tag{59}$$

where, γ is the rake angle of the cutting tool and r is the cutting ratio, i.e. the ratio of the chip thickness to the depth of cut. Since composites display brittle behaviour, it is reasonable to assume that $r \approx 1$ [62]. Using the above

23

315 equations and knowing the area of the shear plane, we obtain the normal and shear strength values used to evaluate failure in the cutting zone as shown in Table 1.

Table 1: Interfacial Normal and shear strength values

θ^o	0	15	30	45	60	75	90
S_σ (N/mm^2)	146.3	103.5	102.9	119.2	143	158.9	183.5
S_τ (N/mm^2)	49.3	26.8	35.2	50.2	71	85.1	113

Generating the failure envelopes for the material under study is performed in order to gain a better understanding of the chip formation mechanisms and

320 how the different failure criteria differ in each loading case. The failure envelope is a 3D closed surface, however, for clarity it is depicted as two 2D graphs: $\sigma_{11} - \sigma_{22}$ envelope is shown in Figure 3a and Figure 3b shows the $\sigma_{22} - \tau_{12}$ envelope. The normal stresses envelope for Max stress and Hashin is identical since $\tau_{12} = 0$. The differences between the failure criteria are clear in Figure 3b.

325 LaRC02 better predicts the beneficial effect of transverse compression on the shear failure which was observed experimentally that Hashin and max stress do not describe.

3.4. Model Set Up

The material is assumed to be in plane stress condition. Positive fibre orien-

330 tation is defined in the same direction as the cutting tool movement. Mechanical properties of the GFRP samples are given in Table 2. In this study, the tool is considered as a rigid body and the thermal effects are not considered. Given that the cutting is performed at low cutting speed, thermal effects are expected to be small. Friction coefficient is made function of fibre orientation as in [63].

335 However, the effect of friction coefficient was found to be minimal due to the termination of the simulation at the completion of the first chip. Other model parameters such as cutting speed, depth of cut, rake and clearance angles were similar to the experimental set up; refer to Table 3.

24

(a) $\sigma_{11} - \sigma_{22}$ at $\tau_{12} = 0$

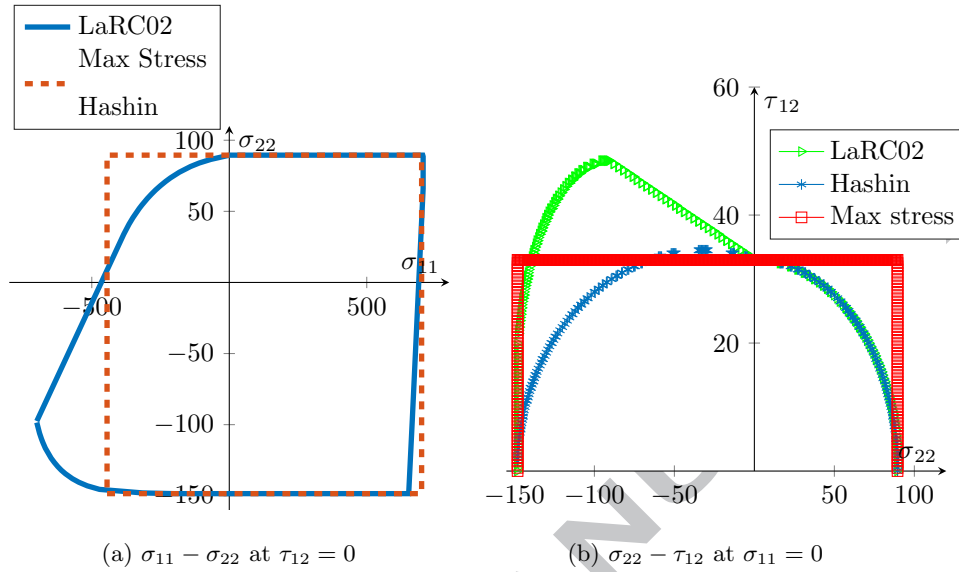(b) $\sigma_{22} - \tau_{12}$ at $\sigma_{11} = 0$

Figure 3: Failure Envelopes for the GFRP samples used in Experiments

3.5. Model settings

³⁴⁰ The number of nodes was set at 13,648; refer to §5.3.using the nodes as vertices for the background mesh resulted in 13,401 cells in the domain and 53,604 Gauss points. These parameters were kept constant throughout the study.
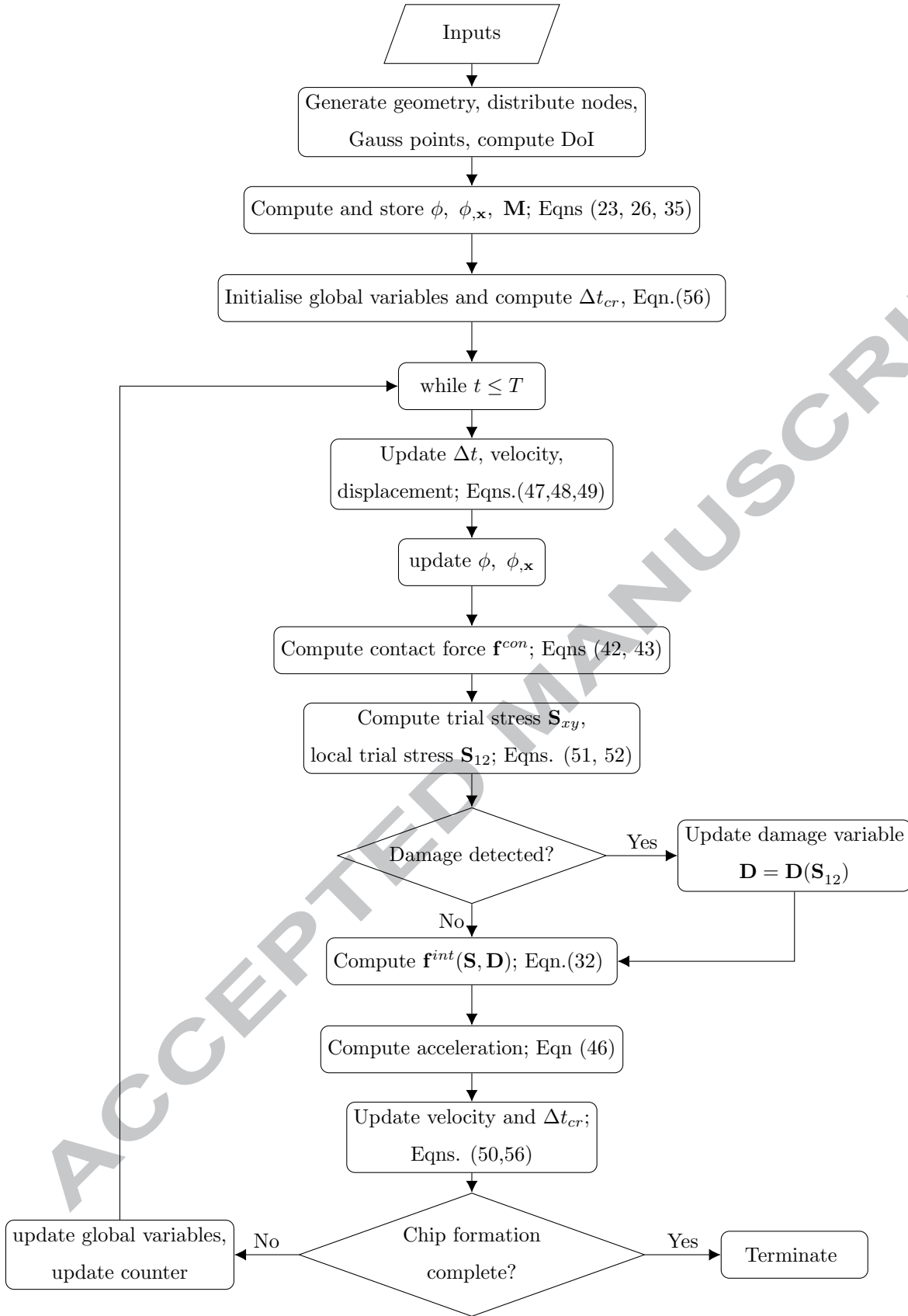
Constructing the meshfree domain of influence (DoI) followed the procedure

³⁴⁵ proposed in [25]. Visibility criterion was used to update DoI of integration points near the chip root (non-convex boundary). This improves the accuracy of the stress field near discontinuities. The analysis was terminated at the completion of the first chip according to the termination criteria in Section 5.4.

3.6. Main algorithm

³⁵⁰ The main algorithm of the dynamic EFG model is shown below. Time integration follows the equations in Section 2.5. The stress is calculated initially in order to update the damage matrix, thus it is called "trial stress". If damage progression occurs during a time step. The stress calculations are repeated in

25

order to accurately calculate $\mathbf{f}^{int}$. The chip formation completion is checked

355 every time step according to the details of Section 5.4.

26

Inputs

Generate geometry, distribute nodes,
Gauss points, compute DoI

Compute and store ϕ, $\phi_{,\mathbf{x}}$, $\mathbf{M}$; Eqns (23, 26, 35)

Initialise global variables and compute Δt_{cr}, Eqn.(56)

while $t \leq T$

Update Δt, velocity,
displacement; Eqns.(47,48,49)

update ϕ, $\phi_{,\mathbf{x}}$

Compute contact force $\mathbf{f}^{con}$; Eqns (42, 43)

Compute trial stress $\mathbf{S}_{xy}$,
local trial stress $\mathbf{S}_{12}$; Eqns. (51, 52)

Damage detected? — Yes → Update damage variable $\mathbf{D} = \mathbf{D}(\mathbf{S}_{12})$

No

Compute $\mathbf{f}^{int}(\mathbf{S}, \mathbf{D})$; Eqn.(32)

Compute acceleration; Eqn (46)

Update velocity and Δt_{cr};
Eqns. (50,56)

Chip formation complete? — Yes → Terminate

No → update global variables,
update counter

4. Experimental Design

4.1. Workpiece Material

The experiments were conducted on Uni-Directional laminates of glass fibre
reinforced plastic (UD-GFRP). Tension, compression and shear tests were performed on specimen of the materials in order to know the material properties which will be used for comparison with modelling results. A minimum of 5 repetitions were carried out to ensure reliable results. The average and standard deviation of the tests are shown in Table 2. A sample of the tests is presented in Figure 4, which shows the tensile test results obtained for seven samples and the average stress-strain curve. As expected, a linear relation is clear for all the specimen.

Table 2: Mechanical properties of the GFRP specimen

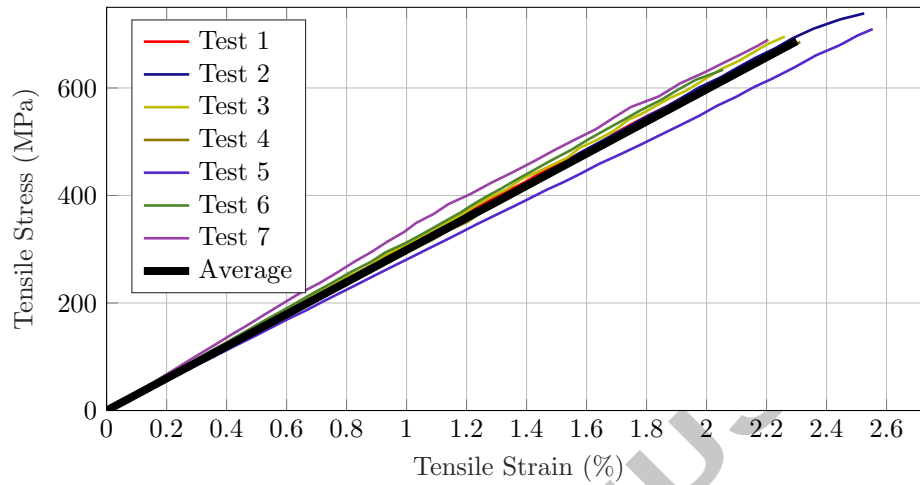| Property	Unit	Mean	Std.
ρ	kg/m^3	1.58	-
E_1	GPa	34.28	2.257
E_2	GPa	11.57	0.496
ν_{12}	-	0.24244	0.037
ν_{21}	-	0.0932	0.007
G_{12}	GPa	2.05	0.207
X^t	MPa	697.8	36.576
Y^t	MPa	89.7216	7.251
X^c	MPa	443.76	66.09
Y^c	MPa	148.33	4.13
S^l	MPa	33.1	2.238
ε_1^t	%	2.3	0.164
ε_2^t	%	1.817	0.121

28

Figure 4: Stress-strain curve during tensile test

4.2. Experimental Design/procedure

Single-point orthogonal cutting experiments were conducted using 3 axis
370   DENFORD vertical CNC machine (VMC 1300 PRO). It has variable feed rate
up to 5000 mm/min. The spindle was locked to prevent rotational movement
during cutting. The cutting speed was controlled by the table feed speed. High
speed steel cutting tools with 0° rake angle were used. The squared-profile tool
is fixed inside the circular tool holder using a specially designed fitting.

375   Ensuring consistent depth of cut throughout the workpiece is essential in
obtaining accurate force measurements. A magnetic base, metric dial gauge is
used to ensure the cut surface is flat within acceptable range of tolerance which
is set to be $\pm 20\mu m$. The dial gauge is fixed on the ceiling of the machine, then
made contact with the top of the workpiece, zeroed and then the workpiece
380   moved slowly while taking readings of the dial. Adjustments to the workpiece
position were made iteratively until the workpiece was appropriately levelled.
The workpiece was fixed sideways in order to investigate the effect of fibre orien-
tation. This was achieved using bespoke clamp. The clamp was fixed on top of
a triaxial force piezo-electric dynamo-meter (Kistler 9257B). The dynamometer
385   was connected with charge amplifier, data acquisition device and PC to collect
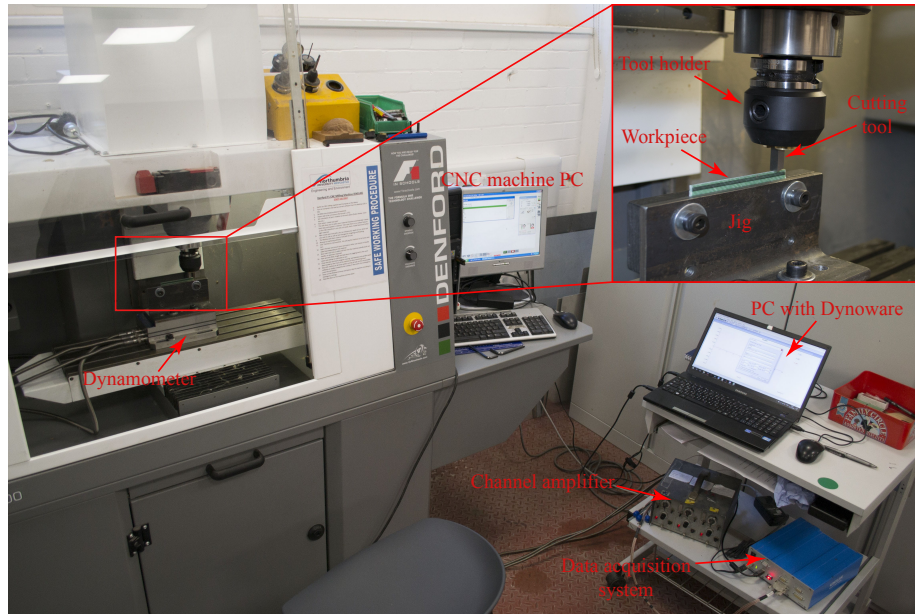
29

Figure 5: Experimental set up

and analyse the force signals. Three repetitions of every test were carried out in order to ensure reliable force readings. The experimental set up is shown in Figure 5 and the running parameters are shown in Table 3.

Table 3: Experimental set up parameters

Process parameters	Units	Levels
Speed	mm/min	3800
Rake Angle	Deg	0
Depth of Cut	mm	0.25
Fibre Orientation	Deg	0, 15, 30, 45, 60, 75, 90

5. Results and Discussion

390 *5.1. Effect of Failure Criteria on Cutting Forces*[1]

Table 4 shows the comparison of the normalised mean cutting force between the EFG model with different failure criteria and the experiments for the range $15^o \leq \theta \leq 75^o$. The experimental values had a minimum of $32.6 \pm 1.6 N/mm$ at $\theta = 15^o$ and maximum of $61 \pm 1.53 N/mm$ at $\theta = 75^o$. Forces using Maximum

395 stress failure ranged from minimum of $27.6 N/mm$ at $\theta = 30^o$ to maximum of $56.8 N/mm$ at $\theta = 75^o$. Force using Hashin failure ranged from minimum of $36.3 N/mm$ at $\theta = 30^o$ to maximum of $50.1 N/mm$ at $\theta = 75^o$. Force using LaRC02 failure ranged from minimum of $30.3 N/mm$ at $\theta = 30^o$ to maximum of $58.5 N/mm$ at $\theta = 75^o$. Maximum deviation from experimental force range

400 was $3.2 N/mm$ using LaRC02 at $\theta = 15^o$, while for Hashin it was $9.6 N/mm$ at $\theta = 75^o$ and for Maximum stress, it was $5.1 N/mm$ at $\theta = 30^o$. This indicates that LaRC02 generated results closest to experimental data within the studied range.

Table 4: Cutting force comparison between model and experiments with different failure criteria

θ^o	$F_c(N/mm)$			
	Max stress	*Hashin*	*LaRC02*	*Experiments*
15	31.4	39.4	37.4	32.6 ±1.60
30	27.6	36.3	30.3	34.5 ±1.87
45	36.7	41.6	43.9	42.3 ±4.14
60	48.6	49.7	50.3	53.5 ±7.43
75	56.8	50.1	58.5	61 ±1.53

Table 5 shows thrust force comparison. It is clear that the model significantly

405 under-estimated the thrust force throughout the studied range. The force val-

---

[1]Note on terminology: In this work, cutting forces are the main cutting force F_c and thrust force F_t. However, when discussed individually, we shall refer to F_c as the cutting force.

ues tended to increase with increased orientation angle. This might be due to the combined effect of increasing friction coefficient and cutting force magnitude at higher orientations. The expeirmental values showed little variation in the thrust force across the studied range (when taking the error bounds into

410 account). The experimental values ranged between 16.9 to 19.2N/mm. Force calculated with maximum stress ranged between 0.9 to 5.6N/mm. Force calculated using Hashin were between 1.6 to 4.1N/mm and using LaRC02 ranged between 2.1 to 5.5N/mm. This significant under-estimation of the thrust force is seen throughout modelling of machining composite literature, across different

415 numerical schemes e.g. [25, 29, 35, 33]. This indicates that it is not related to the choice of meshfree methods, rather it is more related to the difficulties in accurately modelling the composites behaviour under machining conditions. In the current study, two reasons may have contributed to the low thrust force values. Firstly, starting the machining process within the workpiece rather than

420 the free edge. This set up was chosen for numerical stability reasons. Secondly, terminating the simulation after the completion of the first chip. This reduced the bouncing back effect (bouncing back of the machined surface and exerting vertical reaction force on the clearance face of the cutting tool), which was identified as important contributor to the thrust force magnitude in composites

425 machining [62, 33, 29]. Clearly this is an area where significant improvement is required by implementing better constitutive models and material separation criteria.

Table 5: Thrust force comparison between model and experiments with different failure criteria

θ^o	$F_t(N/mm)$			
	Max stress	Hashin	LaRC02	Experiments
15	0.9	2.3	2.7	19.2 ±0.66
30	1	1.6	2.1	16.9 ±0.96
45	2.4	2.7	2.9	17.3 ±1.65
60	4.1	3.1	3.5	18.0 ±1.09
75	5.6	4.1	5.5	18.5 ±3.10

5.2. Mechanisms of Chip formation

The study of chip formation is essential in shedding light on the mechanisms
430 of cutting. Machining models provide a valuable tool in analysing the chip
formation process that is difficult to conduct experimentally such as obtaining
the failure stresses and failure modes. Figures [6, 7, 8, 9] show the progression
of the fibre and matrix failure at $\theta = 30^o$, 75° at the beginning of cutting (left
figures), halfway (middle figures) and near the end of the chip formation (right
435 figures). Each row represents a different failure criteria: top (max stress), middle
(Hashin) and bottom (LaRC02). It is worth noting that the chip formation was
complete at slightly different intervals between the different failure criteria but
time was normalised for each individual case for ease of comparison.

Fibre failure at $\theta = 30^o$ is shown in Figure 6. It is noted that the maximum
440 stress did not predict any significant fibre damage. This is due to the uncoupling
of the shear effects, which plays an important role in reducing the failure stress
of the material. Hashin failure predicts moderate fibre failure along a narrow
band of the chip boundaries. This due to the effect of shear stress on the failure
stress as the location of fibre failure coincides with high shear stresses. This
445 means that the completion of chip formation in Hashin is due to fibre failure
since matrix failure has been completed already (refer to Figure 7f). As for
LaRC02, a substantial fibre damage is predicted in the chip. This is mainly
due the different way of calculating fibre failure under compression. LaRC02

33

predicts fibre fails under compression due to formation of kink bands resulting

⁴⁵⁰ from shear deformation. The kink generates misalignment in the fibres and leads to damage in the fibre and the nearby supporting matrix. This is expected to be dominant failure at lower fibre orientations and 0° rake angle as the rake face directly engages with the workpiece causing severe compressive load on the fibres. Naturally, this loading will propagate along the fibre direction and will

⁴⁵⁵ cause the observed severe damage.

Figure 7 shows the progression of matrix failure at $\theta = 30^o$. The matrix failure starts early near the end of the tool nose and quickly propagates along the fibre directions towards the free surface. A wide band of failure emanating from the rake face towards the free surface is observed due to the high compressive

⁴⁶⁰ stresses exerted by the 0° rake tool. The completion of the chip formation is characterised by almost complete damage in the chipped area. Furthermore, the damage is extended in the machined surface along the fibre direction to a small depth. This is consistent with experimental evidence that cutting at small angles produces good finished surface of the uni-directional composites [64]. The chip

⁴⁶⁵ formation is qualitatively similar for all the failure criteria. However, LaRC02 predicted less matrix damage in the chip. This is due to the increased shear strength at high compressive load in the matrix direction. (Compare second quadrant in Figure 3b).

Figure 8 shows the fibre failure at $\theta = 75^o$. Similarly to Figure 6, maximum

⁴⁷⁰ stress failure criteria predicted negligible failure at the chip root. Hashin and LaRC02 predicted limited failure of the fibre perpendicular to the fibre orientation. This is confirmed experimentally in [4]. The matrix damage is shown in Figure 9. The chip is smaller than in the case of $\theta = 30^o$. This is noted experimentally in [28] and explained by the change in the main failure mechanisms

⁴⁷⁵ from bending of the fibres to brittle crushing. The damage extends to the entire chip in this case due to the non-positive rake angle. Ahead of the complete chip a large area of damaged workpiece. Damage to the machined surface is also larger than in the case of $\theta = 30^o$. It is noted that the damaged area is similar using the different failure criteria. This can be explained with the help of Figure
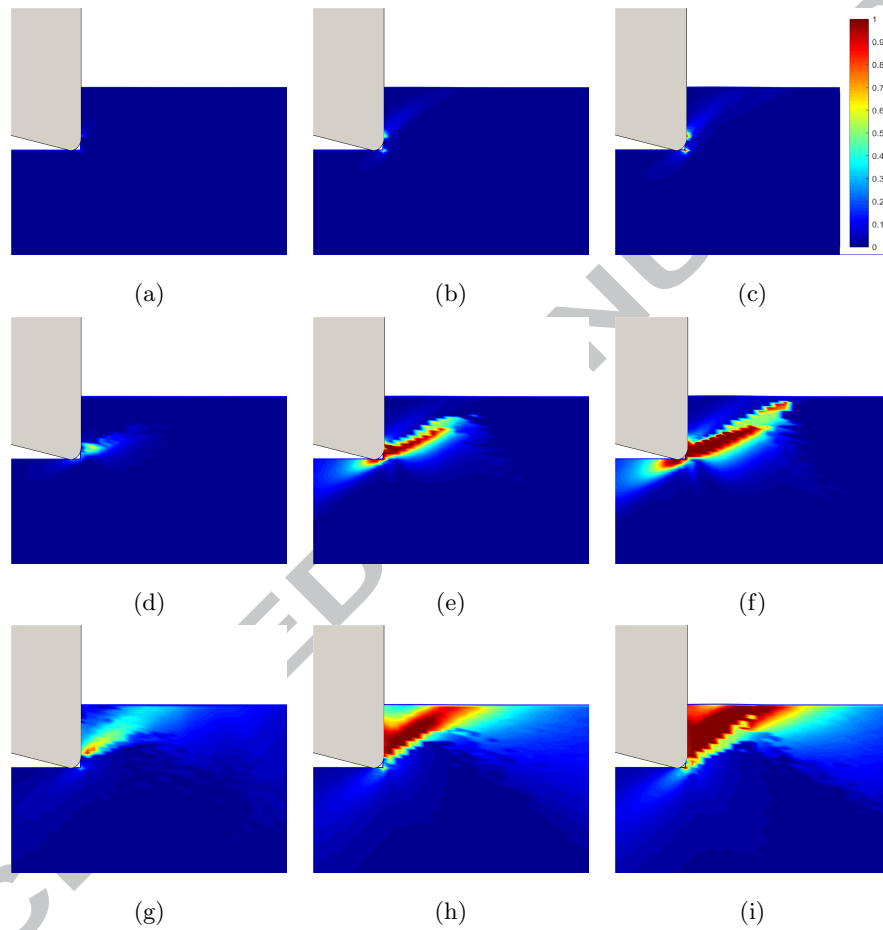
34

Figure 6: Fibre damage progression at $\theta = 30^o$ using maximum stress (a, b, c), Hashin (d, e, f) and LaRC02 (g, h, i)
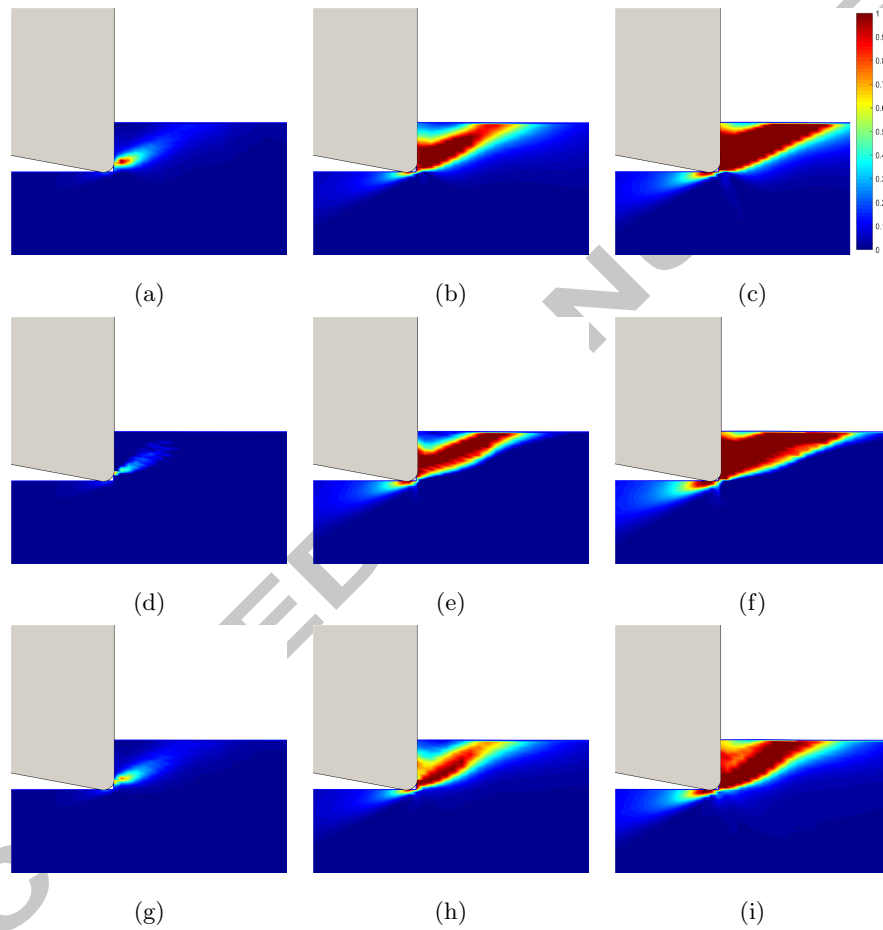
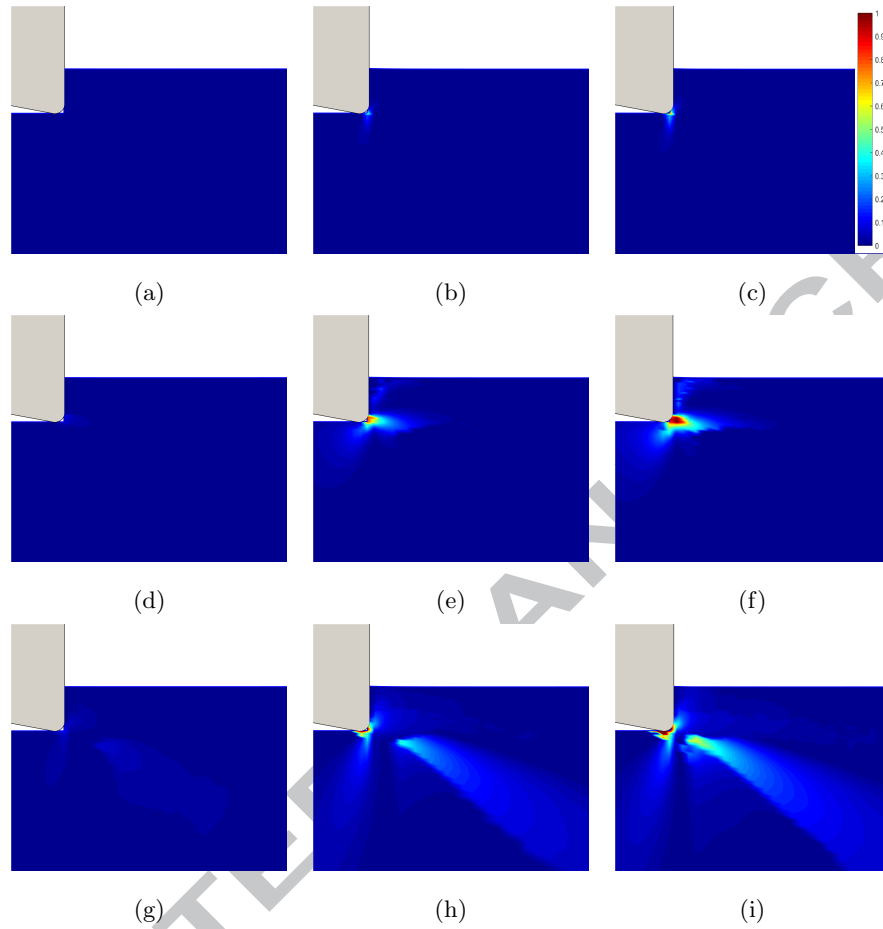Figure 7: Matrix Damage at $\theta = 30^o$ for different failure criteria

Figure 8: Fibre Damage at $\theta = 75^o$ for different failure criteria

3b by noting that at high fibre orientations, the ratio $\dfrac{-\sigma_{22}}{\tau_{12}}$ increases. This will cause the stress evolution to follow a path closer to the negative σ_{22} axis. At this region the three failure envelopes are close to each other.

5.3. Effect of Nodal Density on Cutting Forces

A study of the nodal density effect on the cutting forces is carried out in order to determine the minimum number of nodes that would give a satisfactory results. Table 6 shows cutting force convergence against the number of nodes.
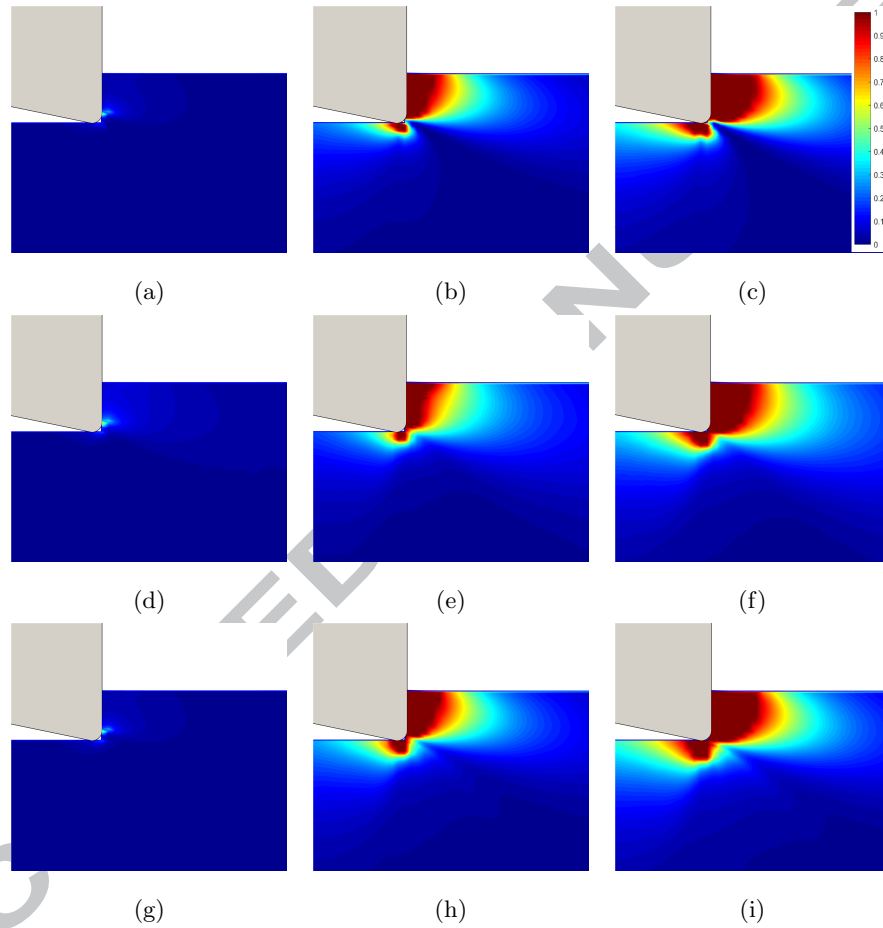
37

(a)　　　　　　　(b)　　　　　　　(c)

(d)　　　　　　　(e)　　　　　　　(f)

(g)　　　　　　　(h)　　　　　　　(i)

Figure 9: Matrix Damage at $\theta = 75^o$ for different failure criteria

38

Table 6: Cutting force convergence against the number of nodes

N	2592	4868	7876	11521	13648	15955
F_c (N/mm)	80.6	63.9	55.5	50.8	48.3	48.3

It is clear that convergence approaches the accurate force value from the top since the model is usually stiffer when it contains lesser number of nodes. $N = 13,648$ is chosen for the simulations throughout the study, since it is the minimum number that achieve convergence.

5.4. Termination Criteria

Completion of the chip formation in orthogonal cutting is usually characterised by material damage propagating from the cutting point (in 2D) to the free surface. Detection of completion of chip formation is somewhat complicated and requires intensive geometrical calculations that add to the computational cost of the code. In this study, a numerical approach utilising the critical time step is devised to predict the completion of the chip without resorting to burdensome geometrical calculations. It was noted that the completion of the chip is detectable from a sudden drop in the critical time step. This is due to the loss of stiffness in the chip as it becomes completely damaged. This in turn will induce sudden large displacement causing the nodes along the chipping plane to get closer and thereby causing significant drop in the time step (refer to Eqn 56). This effect is shown in Figure 10, where the timestep remains nearly constant until the chip completion where the force diverges due to high displacements of the contact surface between the tool and workpiece. In the algorithm 3.6, the gradient of the critical time step is calculated at every time step, when the sudden drop is detected, the code terminates.
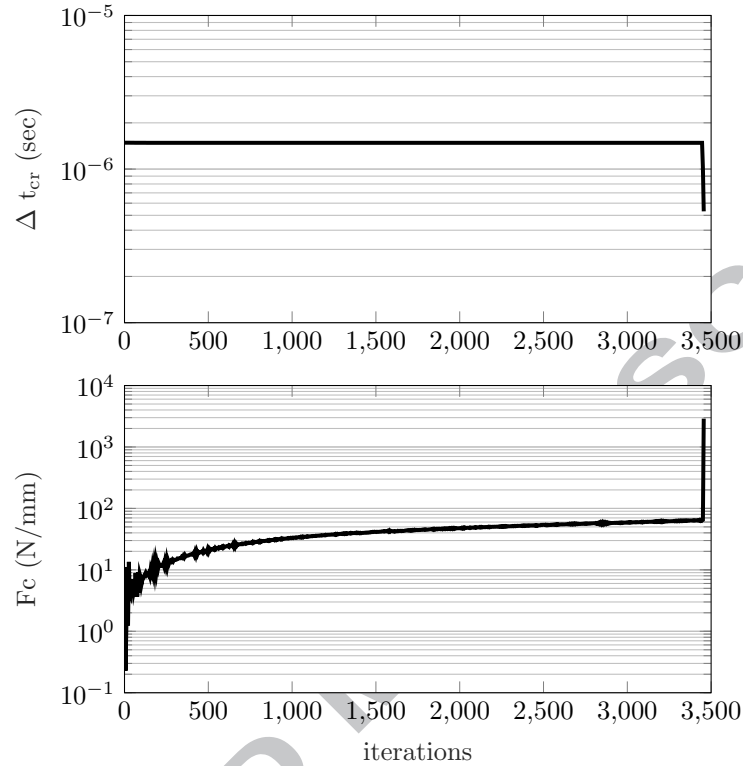
Figure 10: Detection of chip formation completion from gradient of critical time step

6. Summary and Conclusions

This paper presented a novel explicit Element-Free Galerkin Model to simu-
510 late the dynamic orthogonal cutting of unidirectional composites. The discrete
system equations were derived from the virtual work principle and nonlinear
analysis was handled using Updated Lagrangian approach. An orthotropic
Kirchhoff material model combined with option of three different failure cri-
teria were used to model the material behaviour. LaRC02 failure criteria, which
515 has not been used before in composite machining simulations, was found to give
a better accuracy in cutting force prediction as well as to capture important
fibre failure modes that were not predicted by Hashin or Maximum stress cri-
teria. Frictional contact calculations were handled by a novel algorithm using

40

central differencing at the contact nodes. The proposed method avoided the
selection of numerical parameters as in the penalty method while not increasing
the unknowns as in Lagrange multiplier. Another advantage is that the same
algorithm reduces to penalty formulation that can be used in implicit numerical
analysis.

The model results were compared with experimental evidence of orthogonal
cutting at 0° rake angle and fibre orientations $15^o \leq \theta \leq 75^o$. It was found
that the cutting force was predicted with good accuracy for all the failure mod-
els; however, thrust force was significantly under-estimated by the model. This
maybe due to the inability to capture the bouncing back effect and terminat-
ing the analysis at the completion of the first chip. Chip formation analysis
confirmed that the chip separation occurred along the direction of fibres. This
means that the cutting plane coincides with fibre directions in the studied range.
The model can be extended to study other operating and material parameters
such as rake angles, fibre orientations, cutting speeds. The range of study was
limited here by the availability of reliable experimental data for validation.

Comparison between the steady-state machining model of earlier work by
the authors [25] and the current dynamic model highlights several differences:
The proposed model is capable of modelling high speed machining by taking
the inertial effects into account. This extends the applicability of the model
to realistic speeds while maintaining accuracy. Furthermore, chip formation is
better studied with the dynamic model rather than the steady-state model. The
dynamic model is equipped with more advanced material modelling and more
efficient meshfree algorithm with direct imposition of boundary conditions. On
the other hand, the steady-state model is less computationally intensive. This
can be attributed to the very small time step required to maintain the numerical
stability of the dynamic model. The advantages of using meshfree methods
is clear in both models, such as easy and automatic pre-processing and high
quality approximation of field variables. The model can be improved by using
multiphase modelling rather than using the equivalent homogeneous material,
also by including the thermal and strain-rate effects when modelling high speed

41

550 machining.

Acknowledgement

References

555 [1] C. R. Dandekar, Y. C. Shin, Modeling of machining of composite materials: a review, International Journal of Machine tools and manufacture 57 (2012) 102–121.

[2] J. Y. Sheikh-Ahmad, Machining of polymer composites, Springer, 2009.

[3] G. Caprino, A. Langella, Analysing cutting forces in machining processes 560 for polymer-based composites, Machining Technology for Composite Materials: Principles and Practice (2011) 75.

[4] D. Arola, M. Ramulu, D. Wang, Chip formation in orthogonal trimming of graphite/epoxy composite, Composites Part A: applied science and manufacturing 27 (2) (1996) 121–133.

565 [5] H. Takeyama, N. Iijima, Machinability of glassfiber reinforced plastics and application of ultrasonic machining, CIRP Annals-Manufacturing Technology 37 (1) (1988) 93–96.

[6] T. Belytschko, Y. Y. Lu, L. Gu, Element-free galerkin methods, International journal for numerical methods in engineering 37 (2) (1994) 229–256.

570 [7] L. B. Lucy, A numerical approach to the testing of the fission hypothesis, The astronomical journal 82 (1977) 1013–1024.

[8] C. A. Duarte, J. T. Oden, Hp clouds-an hp meshless method, Numerical methods for partial differential equations 12 (6) (1996) 673–706.

42

[9] W. K. Liu, S. Jun, Y. F. Zhang, Reproducing kernel particle methods, International journal for numerical methods in fluids 20 (8-9) (1995) 1081–1106.

[10] G. Liu, K. Dai, K. Lim, Y. Gu, A radial point interpolation method for simulation of two-dimensional piezoelectric structures, Smart Materials and Structures 12 (2) (2003) 171.

[11] L. Dinis, R. N. Jorge, J. Belinha, Analysis of 3d solids using the natural neighbour radial point interpolation method, Computer Methods in Applied Mechanics and Engineering 196 (13-16) (2007) 2009–2028.

[12] L. Dinis, R. N. Jorge, J. Belinha, Analysis of plates and laminates using the natural neighbour radial point interpolation method, Engineering Analysis with Boundary Elements 32 (3) (2008) 267–279.

[13] J. Belinha, L. Dinis, R. Natal Jorge, The natural radial element method, International Journal for Numerical Methods in Engineering 93 (12) (2013) 1286–1313.

[14] J. Belinha, L. Dinis, R. N. Jorge, Composite laminated plate analysis using the natural radial element method, Composite Structures 103 (2013) 50–67.

[15] J.-S. Chen, M. Hillman, S.-W. Chi, Meshfree methods: progress made after 20 years, Journal of Engineering Mechanics 143 (4) (2017) 04017001.

[16] C. Du, An element-free galerkin method for simulation of stationary two-dimensional shallow water flows in rivers, Computer methods in applied mechanics and engineering 182 (1) (2000) 89–107.

[17] G. Li, T. Belytschko, Element-free galerkin method for contact problems in metal forming analysis, Engineering Computations 18 (1/2) (2001) 62–78.

[18] A. Graça, R. P. Cardoso, J. W. Yoon, Subspace analysis to alleviate the volumetric locking in the 3d solid-shell efg method, Journal of computational and applied mathematics 246 (2013) 185–194.

43

[19] L. Liu, L. Chua, D. Ghista, Element-free galerkin method for static and dynamic analysis of spatial shell structures, Journal of sound and vibration 295 (1) (2006) 388–406.

[20] J. Belinha, L. Dinis, Analysis of plates and laminates using the element-free galerkin method, Computers & structures 84 (22) (2006) 1547–1559.

[21] J. Belinha, L. Dinis, Nonlinear analysis of plates and laminates using the element free galerkin method, Composite structures 78 (3) (2007) 337–350.

[22] J. Belinha, A. Araújo, A. Ferreira, L. Dinis, R. N. Jorge, The analysis of laminated plates using distinct advanced discretization meshless techniques, Composite Structures 143 (2016) 165–179.

[23] D. Iliescu, D. Gehin, I. Iordanoff, F. Girot, M. Gutiérrez, A discrete element method for the simulation of cfrp cutting, Composites Science and Technology 70 (1) (2010) 73–80.

[24] I. Shchurov, A. Nikonov, I. Boldyrev, D. Ardashev, Sph modeling of chip formation in cutting unidirectional fiber-reinforced composite, Russian Engineering Research 36 (10) (2016) 883–887.

[25] F. Kahwash, I. Shyha, A. Maheri, Meshfree formulation for modelling of orthogonal cutting of composites, Composite Structures 166 (2017) 193–201.

[26] D. Arola, M. Ramulu, Orthogonal cutting of fiber-reinforced composites: a finite element analysis, International journal of mechanical sciences 39 (5) (1997) 597–613.

[27] N. Bhatnagar, D. Nayak, I. Singh, H. Chouhan, P. Mahajan, Determination of machining-induced damage characteristics of fiber reinforced plastic composite laminates, Materials and Manufacturing Processes 19 (6) (2004) 1009–1023.

44

[28] D. Nayak, N. Bhatnagar, P. Mahajan, Machining studies of uni-directional glass fiber reinforced plastic (ud-gfrp) composites part 1: effect of geometrical and process parameters, Machining science and technology 9 (4) (2005) 481–501.

[29] L. Lasri, M. Nouari, M. El Mansori, Modelling of chip separation in machining unidirectional frp composites by stiffness degradation concept, Composites Science and Technology 69 (5) (2009) 684–692.

[30] A. Mkaddem, I. Demirci, M. E. Mansori, A micro–macro combined approach using fem for modelling of machining of frp composites: cutting forces analysis, Composites science and technology 68 (15) (2008) 3123–3127.

[31] G. Rao, P. Mahajan, N. Bhatnagar, Three-dimensional macro-mechanical finite element model for machining of unidirectional-fiber reinforced polymer composites, Materials Science and Engineering: A 498 (1) (2008) 142–149.

[32] A. Mkaddem, M. El Mansori, Finite element analysis when machining ugf-reinforced pmcs plates: Chip formation, crack propagation and induced-damage, Materials & Design 30 (8) (2009) 3295–3302.

[33] C. Santiuste, X. Soldani, M. H. Miguélez, Machining fem model of long fiber composites for aeronautical components, Composite structures 92 (3) (2010) 691–698.

[34] C. Santiuste, H. Miguélez, X. Soldani, Out-of-plane failure mechanisms in lfrp composite cutting, Composite Structures 93 (11) (2011) 2706–2713.

[35] X. Soldani, C. Santiuste, A. Muñoz-Sánchez, M. Miguélez, Influence of tool geometry and numerical parameters when modeling orthogonal cutting of lfrp composites, Composites Part A: Applied Science and Manufacturing 42 (9) (2011) 1205–1216.

45

[36] K. A. Calzada, S. G. Kapoor, R. E. DeVor, J. Samuel, A. K. Srivastava,
Modeling and interpretation of fiber orientation-based failure mechanisms
in machining of carbon fiber-reinforced polymer composites, Journal of
Manufacturing Processes 14 (2) (2012) 141–149.

[37] S. Usui, J. Wadell, T. Marusich, Finite element modeling of carbon fiber
composite orthogonal cutting and drilling, Procedia CIRP 14 (2014) 211–
216.

[38] S. Zenia, L. B. Ayed, M. Nouari, A. Delamézière, Numerical analysis of
the interaction between the cutting forces, induced cutting damage, and
machining parameters of cfrp composites, The International Journal of Ad-
vanced Manufacturing Technology 78 (1-4) (2015) 465–480.

[39] S. Zenia, L. B. Ayed, M. Nouari, A. Delamézière, An elastoplastic con-
stitutive damage model to simulate the chip formation process and work-
piece subsurface defects when machining cfrp composites, Procedia CIRP
31 (2015) 100–105.

[40] G. Venu Gopala Rao, P. Mahajan, N. Bhatnagar, Machining of ud-gfrp
composites chip formation mechanism, Composites science and technology
67 (11) (2007) 2271–2281.

[41] G. Rao, P. Mahajan, N. Bhatnagar, Micro-mechanical modeling of ma-
chining of frp composites–cutting force analysis, Composites science and
technology 67 (3) (2007) 579–593.

[42] C. R. Dandekar, Y. C. Shin, Multiphase finite element modeling of machin-
ing unidirectional composites: prediction of debonding and fiber damage,
Journal of Manufacturing Science and Engineering 130 (5) (2008) 051016.

[43] A. Abena, S. L. Soo, K. Essa, Modelling the orthogonal cutting of ud-
cfrp composites: Development of a novel cohesive zone model, Composite
Structures 168 (2017) 65–83.

46

[44] D. Nayak, N. Bhatnagar, P. Mahajan, Machining studies of ud-frp composites part 2: finite element analysis, Machining Science and Technology 9 (4) (2005) 503–528.

[45] T. Belytschko, M. Fleming, Smoothing, enrichment and contact in the element-free galerkin method, Computers & Structures 71 (2) (1999) 173–195.

[46] S. Li, D. Qian, W. K. Liu, T. Belytschko, A meshfree contact-detection algorithm, Computer methods in applied mechanics and engineering 190 (24) (2001) 3271–3292.

[47] S. Xiong, J. Rodrigues, P. Martins, Application of the element free galerkin method to the simulation of plane strain rolling, European Journal of Mechanics-A/Solids 23 (1) (2004) 77–93.

[48] T. Belytschko, W. K. Liu, B. Moran, K. Elkhodary, Nonlinear finite elements for continua and structures, John wiley & sons, 2013.

[49] R. De Borst, M. A. Crisfield, J. J. Remmers, C. V. Verhoosel, Nonlinear finite element analysis of solids and structures, John Wiley & Sons, 2012.

[50] T. Belytschko, Y. Krongauz, D. Organ, M. Fleming, P. Krysl, Meshless methods: an overview and recent developments, Computer methods in applied mechanics and engineering 139 (1) (1996) 3–47.

[51] J. Dolbow, T. Belytschko, An introduction to programming the meshless element f reegalerkin method, Archives of Computational Methods in Engineering 5 (3) (1998) 207–241.

[52] T. Most, C. Bucher, A moving least squares weighting function for the element-free galerkin method which almost fulfills essential boundary conditions, Structural Engineering and Mechanics 21 (3) (2005) 315–332.

[53] N.-H. Kim, Introduction to nonlinear finite element analysis, Springer, 2012.

47

[54] G. T. Camacho, M. Ortiz, Computational modelling of impact damage in brittle materials, International Journal of solids and structures 33 (20-22) (1996) 2899–2938.

[55] G.-R. Liu, Meshfree methods: moving beyond the finite element method, CRC press, 2010.

[56] T. Belytschko, W. K. Liu, B. Moran, Nonlinear finite elements for continua and structures, John Wiley & Sons, 2000.

[57] C. G. Dávila, P. P. Camanho, Failure criteria for frp laminates in plane stress, NASA TM 212663 (613).

[58] A. Puck, H. Schürmann, Failure analysis of frp laminates by means of physically based phenomenological models, Composites Science and Technology 58 (7) (1998) 1045–1067.

[59] Z. Hashin, Failure criteria for unidirectional fiber composites, Journal of applied mechanics 47 (2) (1980) 329–334.

[60] Z.-H. Zhong, Finite element procedures for contact-impact problems, Oxford university press, 1993.

[61] V. Laš, R. Zemčík, Progressive damage of unidirectional composite panels, Journal of Composite Materials 42 (1) (2008) 25–44.

[62] L. C. Zhang, H. J. Zhang, X. M. Wang, A force prediction model for cutting unidirectional fibre-reinforced plastics, Machining Science and Technology 5 (3) (2001) 293–305. doi:10.1081/MST-100108616.

[63] A. Mkaddem, M. El Mansori, Finite element analysis when machining ugf-reinforced pmcs plates: Chip formation, crack propagation and induced-damage, Materials & Design 30 (8) (2009) 3295–3302.

[64] N. Bhatnagar, N. Ramakrishnan, N. Naik, R. Komanduri, On the machining of fiber reinforced plastic (frp) composite laminates, International Journal of Machine Tools and Manufacture 35 (5) (1995) 701–716.

48

Appendix A: Summary of Equations of Failure Criteria

In the following failure criteria, the normalised failure index d_i^k varies between 0 (no failure) and 1 (total failure). For each integration point, two or three values are calculated and stored in the damage matrix $\mathbf{D}$ using one of the below failure criteria.

Maximum stress

<u>For fibre tension $\sigma_1 > 0$</u>

$$d_f^t = \left(\frac{\sigma_1}{X^t}\right)^2 \leq 1$$

where, X^t is the tensile strength in fibre direction.

<u>For fibre compression $\sigma_1 < 0$</u>

$$d_f^c = \left(\frac{\sigma_1}{X^c}\right)^2 \leq 1$$

where, X^c is the compressive strength in fibre direction.

<u>For matrix cracking $\sigma_2 > 0$</u>

$$d_m^t = \left(\frac{\sigma_2}{Y^t}\right)^2 \leq 1$$

where, Y^t is the tensile strength in transverse direction.

<u>For matrix crushing $\sigma_2 < 0$</u>

$$d_m^c = \left(\frac{\sigma_2}{Y^c}\right)^2 \leq 1$$

where, Y^c is the compressive strength in transverse direction.

<u>For shear failure</u>

$$d_s = \left(\frac{\tau_{12}}{S^l}\right)^2 \leq 1$$

where, S^l is the in-plane longitudinal shear strength.

Hashin

<u>For fibre tension $\sigma_1 > 0$</u>

$$d_f^t = \left(\frac{\sigma_1}{X^t}\right)^2 + \left(\frac{\tau_{12}}{S^l}\right)^2 \leq 1$$

49

For fibre compression $\sigma_1 < 0$

$$d_f^c = \left(\frac{\sigma_1}{X^c}\right)^2 \leq 1$$

For matrix cracking $\sigma_2 > 0$

$$d_m^t = \left(\frac{\sigma_2}{Y^t}\right)^2 + \left(\frac{\tau_{12}}{S^l}\right)^2 \leq 1$$

For matrix crushing $\sigma_2 < 0$

$$d_m^c = \left(\frac{\sigma_2}{2S^{tr}}\right)^2 + \left[\left(\frac{Y^c}{2S^{tr}}\right)^2 - 1\right]\frac{\sigma_2}{Y^c} + \left(\frac{\tau_{12}}{S^l}\right)^2 \leq 1$$

where, S^{tr} is the in-plane transverse shear strength.

LaRC02

For matrix tension $\sigma_2 > 0$

$$d_m^t = \left(\frac{\sigma_2}{Y^t}\right)^2 + \left(\frac{\tau_{12}}{S^l}\right)^2$$

For fibre tension $\sigma_1 \geq 0$

$$d_f^t = \frac{\varepsilon_1}{\varepsilon_1^t}$$

For matrix compression $\sigma_2 < 0$ and $\sigma_1 \geq Y^c$

$$d_m^c = \left(\frac{\tau_{\text{eff}}^{\text{T}}}{S^{\text{tr}}}\right)^2 + \left(\frac{\tau_{\text{eff}}^{\text{L}}}{S^{\text{l}}}\right)^2$$

where, $\tau_{\text{eff}}^{\text{T}}$ and $\tau_{\text{eff}}^{\text{L}}$ are the effective stress:

$$\tau_{\text{eff}}^{\text{T}} = \left\langle -\sigma_2 \cos\Upsilon(\sin\Upsilon - \eta^T \cos\Upsilon)\right\rangle$$
$$\tau_{\text{eff}}^{\text{L}} = \left\langle \cos\Upsilon(|\tau_{12}| + \eta^L \sigma_{22} \cos\Upsilon)\right\rangle$$

where, $\langle \cdots \rangle$ is the Macaulay operator, Υ is fracture plane angle and Υ_0 is fracture plane angle in pure transverse compressive loading. The transverse shear strength is given as:

$$S^{tr} = Y^c \cos\Upsilon_0 \left(\sin\Upsilon_0 + \frac{\cos\Upsilon_0}{\tan 2\Upsilon_0}\right)$$

50

The coefficients of transverse and longitudinal influence are given as

$$\eta^T = \frac{-1}{\tan 2\Upsilon_0}$$

$$\eta^L \approx -\frac{S^l \cos 2\Upsilon_0}{Y^c \cos^2 \Upsilon_0}$$

For matrix compression $\sigma_2 < 0$ and $\sigma_1 < Y^c$

$$d_m^c = \left(\frac{\tau_{\text{eff}}^{\text{mT}}}{S^{\text{tr}}}\right)^2 + \left(\frac{\tau_{\text{eff}}^{\text{mL}}}{S^{\text{l}}}\right)^2$$

where, the additional superscript m denotes that the stresses are calculated in the misalignment frame coordinates.

$$\sigma_1^m = \cos^2 \psi \; \sigma_1 + \sin^2 \psi \; \sigma_2 + 2\sin \psi \cos \psi \; \tau_{12}$$

$$\sigma_2^m = \sin^2 \psi \; \sigma_1 + \cos^2 \psi \; \sigma_2 - 2\sin \psi \cos \psi \; \tau_{12}$$

$$\tau_{12}^m = -\sin \psi \cos \psi \; \sigma_1 + \sin \psi \cos \psi \; \sigma_2 + (\cos^2 \psi - \sin^2 \psi) \; \tau_{12}$$

where, ψ is the kink misalignment angle and is given as:

$$\psi = \frac{\tau_{12} + (G_{12} - X^c) \; \psi^c}{G_{12} + \sigma_1 - \sigma_2}$$

$$\psi^c = \tan^{-1} \left(\frac{1 - \sqrt{1 - 4\left(\frac{S^l}{X^c} + \eta^L\right)\left(\frac{S^l}{X^c}\right)}}{2\left(\frac{S^l}{X^c} + \eta^L\right)} \right)$$

For fibre compression $\sigma_1 < 0$ and $\sigma_2^m < 0$

$$d_f^t = \left\langle \frac{|\tau_{12}^m| + \eta^L \sigma_2^m}{S^l} \right\rangle$$

For fibre compression $\sigma_1 < 0$ and $\sigma_2^m \geq 0$

$$d_m^c = \left(\frac{\sigma_2^m}{Y^{\text{tr}}}\right)^2 + \left(\frac{\tau_{12}^m}{S^{\text{l}}}\right)^2$$

51